Chapter 3 Hydrogen Evolution Reaction Study using $MoSe_2$ based Nanomaterials as Electrodes

3.1 Introduction:

Almost 90% of the world's energy supply is now produced by carbon-based fossil fuels. Fossil fuel consumption increases global warming, ozone depletion, ocean acidification, resource depletion, and detrimental environmental issues [84]. These issues have significantly impacted every country's social and economic development along with human, plant, and animal life. Therefore, developing effective methods for producing renewable energy is essential for increasing demand for energy [85]. Owing to this reason, there has been significant progress in converting clean, renewable and sustainable energy such as wind, solar, hydroelectric and biomass to supply electric power and carriers of energy storage. In this regard, green hydrogen gas (H_2), which has a very high calorific value and almost no emissions of dangerous or hazardous gases, has been promoted as one of the most promising sustainable and clean energy sources for ecological systems. Natural gas steam reforming is the primary method used in the industrial sector to produce H_2, but these processes release CO_2 into the atmosphere, compromising the environmental benefits of using H_2 as a fuel. Therefore, achieving sustainable commercial and industrial hydrogen production is a big challenge. Hydrogen production via electrolysis generates 99.9% pure hydrogen with zero emission of CO_2 gas compared to any other production method [9]. This technique has attracted much interest due to cost effectiveness, environmental friendliness, high efficiency and, more importantly, zero percent CO_2 emission. **Figure 3.1** depicts the standard schematics for the breakdown of water into hydrogen and oxygen.

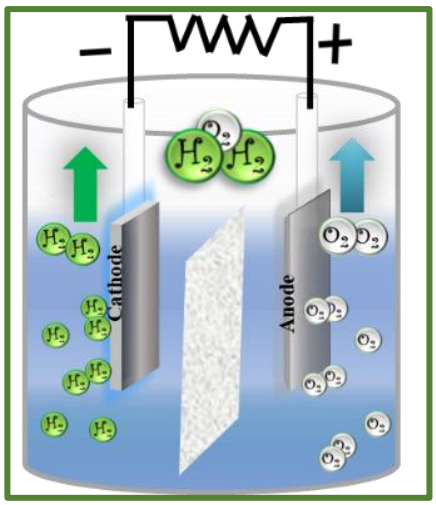

Figure 3.1 *Basic schematic for splitting water into hydrogen and oxygen.*

Generally, noble metal (Pt) is considered the best electrocatalyst for hydrogen production due to its low overpotential and fast kinetics, but the high cost and scarcity hinder the use of these catalysts. Therefore, non-metal catalysts can be required, which becomes economically viable but must overcome the problem of high overpotential (η) in the electrochemical process [10]. Promising electrocatalysts are needed to reduce overpotential values to increase the efficiency and rate of reaction. Sustainable electrocatalysts such as metals, metal oxides, metal dichalcogenides and carbon-based nanostructures, are good choice for better hydrogen production.

The performance of the electrochemical hydrogen evolution reaction (HER) depends on the electrocatalytic activity of electrode materials. In particular, good electrocatalytic activity requires the presence of rich active sites and a suitable surface structure. However, pristine carbon nanostructures do not act as promising electrocatalysts for hydrogen production, but they can work as excellent electrocatalysts after surface modification like functionalization and heterostructure formation. The two-dimensional (2D) transition metal dichalcogenides (TMDs) such as MoS_2, $MoSe_2$, WS_2, WSe_2 etc. have been used as electrocatalysts for hydrogen generation because of their high acidic/basic stability, natural abundance and excellent

electrochemical activity. These TMDs as catalysts can help to lower the energy required to split the water and enhance hydrogen production. This chapter is mainly focused on fundamentals related to HER and use of $MoSe_2$ based nanomaterials as efficient electrocatalysts for HER.

3.1.1 Reactions involved in HER process:

The Gibbs free energy (G^0) of water splitting reaction is 237.2 kJ mol^{-1} under the standard temperature and pressure [86]. The Gibbs free energy can be expressed (**equation 3.1**) in terms of standard cell potential as-

$$\Delta G^0 = -nFE^0 \tag{3.1}$$

Where F is the Faraday constant, n represents the number of transferred electrons per product formed and $E°$ represents the standard cell potential. The enthalpy of water splitting under adiabatic conditions is 286 kJ mol^{-1}. The chemical equation of full water splitting is described by following reaction.

$$2H_2O \rightleftharpoons 2H_2 + O_2 \tag{3.2}$$

Water splitting reaction is divided into two half-cell reactions: Cathodic half-cell reaction (**reactions 3.3, 3.7**) representing proton reduction and anodic half-cell reaction (**reactions 3.5, 3.9**), showing water oxidation reaction [86]. In acidic electrolyte, the following reactions occur for HER.

Reaction at cathode side-

$$2H^+ + 2e^- \rightleftharpoons H_2\,, \quad \text{with} \quad E^0 = 0.00\text{V} \tag{3.3}$$

$$E = E^0 + \frac{0.059}{2} log\,[H^+]^2 = E^0 + 0.059\,log[H^+]$$

$$= 0 - 0.059\,pH \tag{3.4}$$

Reaction at anode side-

$$2H_2O \rightleftharpoons 4H^+ + O_2 + 4e^- \quad \text{with} \quad E^0 = 1.23 \tag{3.5}$$

$$E = E^0 + \frac{0.059}{4} \log\,[H^+]^4 = E^0 + 0.059\,\log[H^+]$$

$$= 1.23 - 0.059\ \text{pH} \quad (3.6)$$

Similar reactions follow for HER in alkaline electrolyte:

Reaction at cathode side-

$$2H_2O + 2e^- \rightleftharpoons H_2 + 2OH^- \quad \text{with} \quad E^0 = -0.83\text{V} \quad (3.7)$$

$$E = E^0 + \frac{0.059}{2}\log [OH^-]^2 = E^0 + 0.059 \log[OH^-]$$

$$= -0.83 - 0.059\ \text{pH} \quad (3.8)$$

Reaction at anode side-

$$4OH^- \rightleftharpoons O_2 + 2H_2O + 4e^- \quad \text{with} \quad E^0 = 0.40\text{V} \quad (3.9)$$

$$E = E^0 + \frac{0.059}{4}\log [OH^-]^4 = E^0 + 0.059 \log[OH^-]$$

$$= 0.40 - 0.059\ \text{pH} \quad (3.10)$$

An external voltage is applied across the electrodes to split water molecules into hydrogen and oxygen. The reversible voltage is computed as 1.23 V at 25 °C, which is the minimum thermodynamic potential required to electrolyze water. Reactions 3.4 and 3.6 show the influence of pH on the potential in an acidic medium, whereas **reactions 3.8 and 3.10** show the influence of pH in an alkaline medium. The Nernst equation reveals that redox potentials shift linearly by -59 mV for each half-reaction. On the other hand, electrochemical processes typically need more energy than thermodynamics estimation.

3.1.2 Reaction mechanism for HER:

The HER is a multi-step electrochemical reaction that takes place on the catalyst surface. The hydrogen evolution process follows two proton-coupled electron transfer mechanisms. The adsorption of proton at the catalyst surface, proton combination, and fast electron transport to the active sites all contribute majorly in this process. The two pathways that govern HER are the Volmer-Heyrovsky and Volmer-Tafel reactions.

3.1.2.1 HER reaction in acidic medium

The HER mechanism in the acidic medium described by Volmer-reaction is explained by Volmer-Heyrovsky or Volmer-Tafel mechanisms, as shown schematically in **Figure 3.2 (a)**.

Volmer Step: A hydronium ion (H_3O^+) transfers from the solution to the catalyst surface during the discharge process (Volmer reaction), combining with a cathodic electron to produce H_{ads} on metal sites as follows-

$$H_3O^+ + e^- + M \rightleftharpoons MH_{ads} + H_2O \quad (3.11)$$

The following two alternative steps can subsequently be taken after Volmer reaction.

Volmer-Heyrovsky step: A H_3O^+ in the solution combines with a proton that has been adsorbed to the catalyst's surface, followed by **reaction 3.12**.

$$MH_{ads} + H_3O^+ + e^- \rightleftharpoons M + H_2 + H_2O \quad (3.12)$$

Volmer-Tafel step: Two H_{ads} in the vicinity combine on the catalyst's surface to give a molecular hydrogen as follows-

$$MH_{ads} + MH_{ads} \rightleftharpoons 2M + H_2 \quad (3.13)$$

The active site of the catalyst is denoted by M, while MH_{ads} represent the adsorbed hydrogen atom at the active site.

3.1.2.2 HER reaction in alkaline medium

In the alkaline medium, breaking the strong covalent H-O-H bonds requires more energy compared to the weak hydronium ion covalent bond in acidic media. Reactions for HER in the alkaline media are sensitive at the catalyst's surface. The HER mechanism (in the alkaline medium) also involves two reaction steps; Volmer-Heyrovsky or Volmer-Tafel mechanisms.

Volmer reaction: Water adsorption takes place in an alkaline medium. The hydrogen adsorbed on the catalyst surface due to the coupling of water and e^-.

$$M + H_2O + e^- \rightleftharpoons MH_{ads} + OH^- \quad (3.14)$$

***Volmer Heyrovsky reaction*:** It is electrochemical desorption in which H_{ads} combine with H_2O molecules.

$$MH_{ads} + H_2O + e^- \rightleftharpoons M + H_2 + OH^- \quad (3.15)$$

***Volmer Tafel reaction*:** Two H_{ads} in the vicinity combine on the surface of the electrocatalyst to give a molecular hydrogen as described in **equation 3.13**.

In overall HER reaction, the adsorption and desorption of hydrogen on the catalyst surface play important role in either acidic or alkaline medium. The source of hydrogen for HER in acidic and basic electrolytes makes a fundamental difference. Where the active intermediates are generated from protons in alkaline electrolytes, extra activation mechanism involving the dissociation of water is necessary to generate the H_{ads} on the catalyst surface [87]. Hydrogen atoms cannot effectively adsorb on the catalyst's surface when the interaction of hydrogen atoms with the catalyst's surface is too weak [88]. When the interaction is strong between the hydrogen atom and the catalyst's surface, it is difficult to dissociate the hydrogen. Therefore, the optimal interaction is required for the adsorption and desorption of the hydrogen.

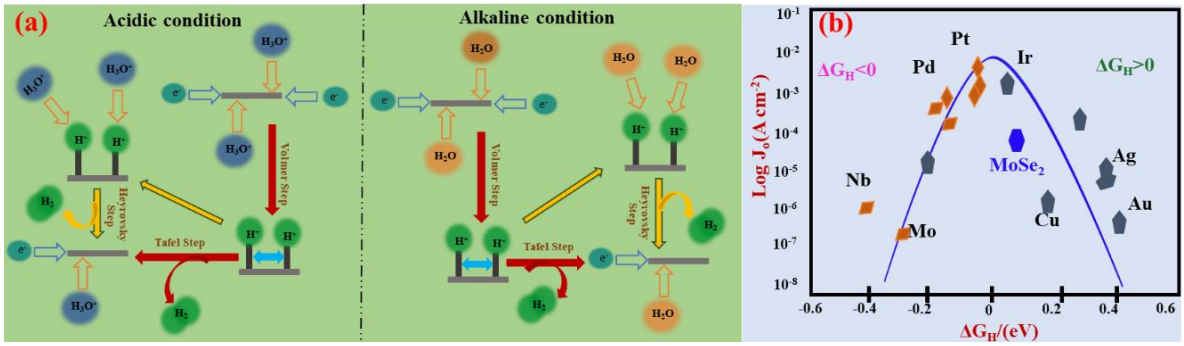

Figure 3.2 *(a) HER mechanism in acidic and alkaline condition, (b) Volcano plot showing probable electrocatalysts for HER.*

The Volcano plot helps to point out the optimal condition for hydrogen adsorption and desorption. As shown in **Figure 3.2 (b)**, the volcano plot shows the maximum exchange current

density for the catalyst where the hydrogen binding Gibbs free energy (ΔG) is minimal or close to zero. The ΔG=0 represents the volcano peak. The catalysts on the left side of the volcano peak (ΔG<0) show the electrocatalyst surface's strong interaction with H^+. The adsorption of the catalyst with H^+ is fast, but desorption is slow. The catalyst on the right side of the volcano peak (ΔG>0) weakly interacts with hydrogen. The catalyst interaction with active sites is weak. Therefore, an electrocatalyst must have minimum free energy (close to zero) and a high exchange current density [89].

3.2 Performance evolution index for electrocatalyst:

The overall electrode activity, overpotential, the Tafel slope, charge transfer resistance and catalytic durability are important parameters that explain the HER catalytic activity of specific electrocatalyst material.

3.2.1 Overpotential (η)

One of the most frequent indicators to determine the catalytic activity of an electrocatalyst is the overpotential (above and beyond the thermodynamic potential), which drives the reaction at a specific scan rate. Overpotential is the minimal potential required to generate the hydrogen from the electrocatalyst surface. The correlation between the overpotential and the overall potential is given by following **equation 3.16**.

$$E_{op} = E_{rev} + iR + \eta \qquad (3.16)$$

Where E_{op} is the overall potential of electrochemical reactions and iR is the ohmic potential drop due to the resistance of ion flow in the electrolyte. The E_{rev} is a reversible thermodynamical potential, and η is an overpotential which is estimated by the polarisation curve evaluated using linear sweep voltammetry (LSV) measurements.

3.2.2 Tafel slope and exchange current density

Tafel slope indicates the rate-determining step of the reaction. The Tafel slope reflects the intrinsic catalytical activity of a catalyst. The Tafel plot indicates a linear relationship between the applied potential and the logarithmic current density (log j), as given in following **equation 3.17**.

$$\eta = b\ logj\ + a \tag{3.17}$$

Where η represents the overpotential, j denotes the current density (mA cm^{-2}) and b is the Tafel slope (mV dec^{-1}). The high current density suggests that the electrode/electrolyte contact may easily transport electrons with a low activation energy. Evidently, an active electrocatalyst should display a low overpotential and a small Tafel slope for excellent hydrogen production.

3.2.3 Electrochemical impedance spectroscopy (EIS) measurements

EIS is used to understand the electrochemical activity of any material or device. In this method, the charge transfer resistance of catalyst and factors directly associated with HER activity can be obtained by applying a small potential perturbation and measuring the resulting current response. In HER, charge transfer resistance represents the hindrance faced by electrons as they participate in the electrochemical reduction of protons to produce hydrogen gas. Higher the charge transfer resistance, the lower the HER performance will be. EIS data is graphically described by Nyquist plot. The Nyquist plot represents three distinct zones in imaginary vs. real impedance curve- an intercept on the real axis (internal resistance R_s), a semicircle in the high-frequency zone (charge transfer resistance R_{ct}), and a constant phase element (Q).

3.3 Electrocatalyst for hydrogen production:

The catalyst's inherent electrochemical behavior and catalytic properties are required to develop more sustainable and low-cost electrocatalysts for hydrogen production. The electrode materials that accelerate reaction rates should have a fast charge transfer rate, maximum active sites, low cost, abundance and sustainability. Metals like Pt, Pd, and Ru-based electrocatalysts

exhibit high activities towards hydrogen production. However, these metals are costly for large-scale production, and their negative environmental effect hinder their practical application. Hence, much work has gone into finding cost-effective, earth-abundant, and catalytically active alternatives. In this regard, different non-precious catalysts such as carbon-based materials, transition metal nitrides, transition metal oxides, transition metal dichalcogenides, transition metal phosphides etc., have been investigated as electrode material for hydrogen production [90].

3.4 Results and discussion

3.4.1 *In-situ* grown $MoSe_2$ over different substrates as binder free electrodes for HER

In this study, we have explored the hydrothermally synthesized in-situ grown $MoSe_2$ over conducting suberates (conducting carbon paper & Ni foam) as binder-free electrodes for HER. This study delves into the characterization and examination of the electrochemical behavior of in-situ vertically grown $MoSe_2$-CCP and $MoSe_2$-Ni foam-based electrodes. To study the HER activity of the prepared samples, we have conducted studies using linear sweep voltammetry (LSV), electrochemical impedance spectroscopy (EIS) and chronoamperometry. Additionally, cyclic voltammetry (CV) techniques have been employed to determine the electrochemical active surface area (ECSA).

3.4.1.1 Characterization of in-situ grown $MoSe_2$ over substrate

The electron microscopy studies of prepared $MoSe_2$ electrodes are done to understand the surface morphology of prepared electrodes. The SEM study reveals that $MoSe_2$ nanostructures have a well-defined, highly dense vertically grown wrinkled architecture with uniform distribution over CCP and Ni foam substrates. **Figure 3.3 (a)** shows the growth of vertical $MoSe_2$ over the fibrous structure of CCP and the higher magnification image (**Figure. 3.3 (b)**) reveals densely packed and well-aligned vertical wrinkled-like structure grown on CCP.

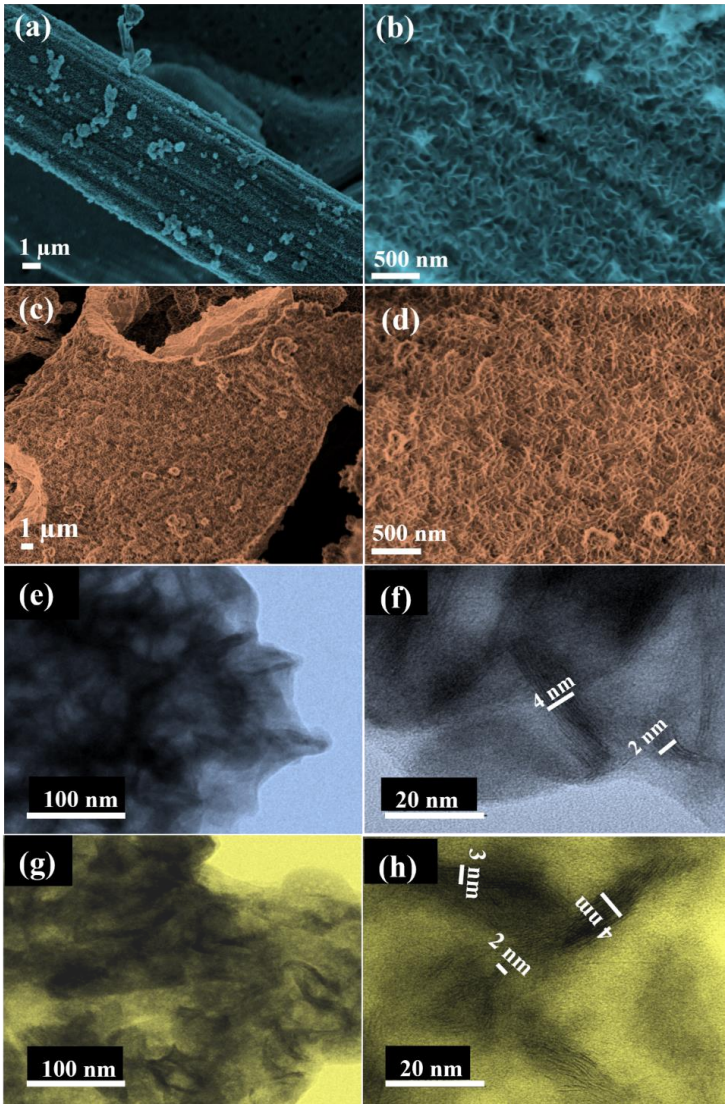

Figure 3.3 *SEM images of (a,b) $MoSe_2$-CCP and (c,d) $MoSe_2$-Ni foam electrodes; TEM and HRTEM images of (e,f) $MoSe_2$-CCP and (g,h) $MoSe_2$-Ni foam electrodes.*

The $MoSe_2$ nanosheets are grown on a substrate and stacked on top of each other, but the van der Waals forces between the nanosheets are not strong enough to prevent them from sliding past each other. This causes the nanosheets to be compressed, which creates a high strain energy and the growth of $MoSe_2$ nanosheets in the vertical direction to the substrate to minimize the strain energy [91]. This leads to the formation of wrinkled like structures of grown $MoSe_2$ nanosheets. Similarly, SEM images (**Figure 3.3 (c,d)**) of $MoSe_2$-Ni foam electrode show the growth of densely packed vertical nanosheets throughout the substrate. Further, the TEM imaging technique is utilized to understand the structure of prepared

samples. **Figure 3.3 (e,f)** show the TEM images for $MoSe_2$-CCP, which clearly demonstrate the formation of wrinkled like structure with each nanosheets thickness in the range of 2-4 nm. Similar observations have been found for $MoSe_2$-Ni foam as well, as shown in **Figure 3.3 (g,h)**.

The X-ray diffraction (XRD) patterns of $MoSe_2$-CCP and $MoSe_2$-Ni foam exhibit diffraction peaks corresponding to various crystallographic planes of the $MoSe_2$ and respective substrates, as shown in **Figure 3.4 (a)**. The peak appearing at ~13.4° for $MoSe_2$-CCP and ~14° for $MoSe_2$-Ni foam, attributes to the (002) diffraction plane of $MoSe_2$ that is perpendicular to the layer structure. This peak position suggests the interlayer spacing of $MoSe_2$, which is typically around 0.66 nm for $MoSe_2$-CCP and 0.63 nm for $MoSe_2$-Ni foam. It has been reported in the literature that depending on the substrate coupling with layered TMDs and the nature of the substrate, the crystalline nature of the synthesized layered materials may differ, leading to peak shift in XRD pattern [92]. The other peaks in $MoSe_2$-CCP at ~33°, ~37.1°and ~55.6° belong to (100), (103) and (110) planes of $MoSe_2$, respectively, while the peak at ~25.6° is attributed to the (002) plane of CCP (JCPDS 20-0757) [93]. The presence of other crystallographic planes of $MoSe_2$ like (100), (103) and (110) is also observed at ~33°, 37.2° and 55.3° for $MoSe_2$-Ni foam, respectively, along with the peaks at 44.6° (111) and 51.9° (200), attributed to the planes of Ni foam substrate. An additional peak at ~29.8° in $MoSe_2$-Ni foam electrode may be due to the possible partial oxidation of Se edges and formation of SeO_x [94]. Raman spectroscopy is utilized for investigating the vibrational properties of prepared vertical $MoSe_2$ based electrodes. Raman spectra for the prepared electrodes are shown in **Figure 3.4 (b)**, which reveal the existence of vibrational modes of $MoSe_2$. The peaks at 238.9 and 285.4 cm^{-1} for $MoSe_2$-CCP and 234.2 and 281.8 for $MoSe_2$-Ni foam depict the in-plane (A_{1g}) and out-of-plane (E^1_{2g}) vibrations of Mo and Se atoms, respectively [73, 79, 95]. FTIR spectra (**Figure 3.4 (c)**) show multiple peaks corresponding to different molecular vibrations in $MoSe_2$-

CCP and $MoSe_2$-Ni foam electrodes. The peaks around 829, 976, 1362, 1625, and 3368 cm^{-1} are belonging to the C-H, O-Mo-O, M=O, C-H, Mo-Se and O-H vibrations, respectively [68, 76, 96, 97].

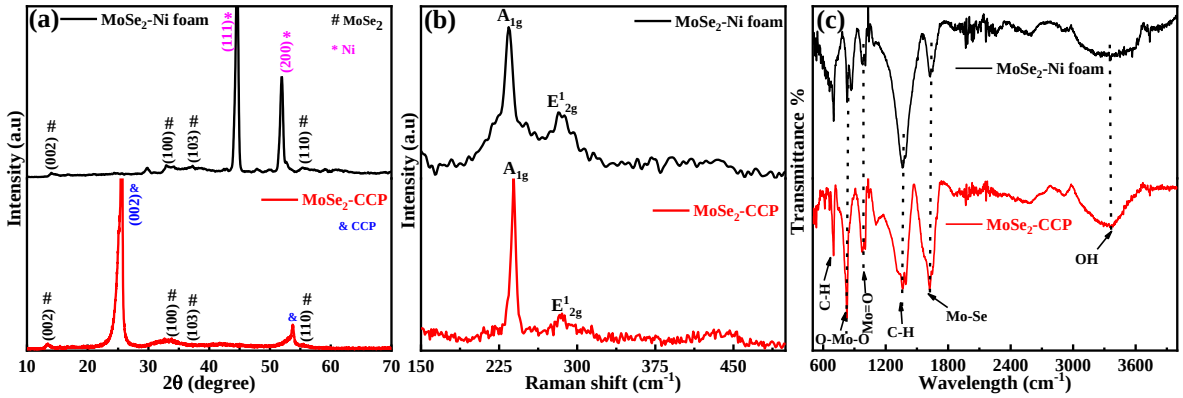

Figure. 3.4 *(a) XRD patterns, (b) Raman and (c) FTIR spectra for $MoSe_2$-CCP and $MoSe_2$-Ni foam.*

X-ray photoelectron spectroscopy (XPS) is a non-destructive surface-sensitive tool to get information about the chemical composition of samples. The survey spectrum obtained for the $MoSe_2$-CCP electrode demonstrates the standard peaks of Mo-3d, Se-3d, O, and C, as shown in **Figure 3.5 (a)**. The Mo-3d spectrum (**Figure 3.5 (b)**) of the $MoSe_2$-CCP electrode has a couple of doublet peaks at 231.0 eV for Mo $3d_{3/2}$ and 228.2 eV for Mo $3d_{5/2}$ corresponding to the metallic 1T phase of $MoSe_2$, and another doublet peaks at energy (231.9 eV for Mo $3d_{3/2}$ and 228.8 eV for Mo $3d_{5/2}$) corresponding to the semiconducting 2H phase of $MoSe_2$, while the peak at 235.85 eV belongs to Mo^{6+}. This observation reveals the formation of hybrid 1T (20%) and 2H (80%) of $MoSe_2$ in $MoSe_2$-CCP electrode [57, 98-100]. Selenium exists in the Se^{2-} form, as seen by the two different peaks in the Se core level XPS spectrum (**Figure 3.5 (c)**), which are located at approximately 54.62 eV ($3d_{5/2}$) and 55.18 eV ($3d_{3/2}$), respectively. Similarly, the survey spectrum of the grown $MoSe_2$-Ni foam electrode demonstrates the presence of the standard peaks of Mo 3d, Se 3d, O, and Ni, as shown in **Figure 3.5 (d)**. The Mo 3d spectrum (**Figure 3.5 (e)**) for $MoSe_2$-Ni foam typically exhibits two doublet peaks at 231.66 eV for Mo $3d_{3/2}$ and 228.33 eV for Mo $3d_{5/2}$ corresponding to metallic (1T) phase of

$MoSe_2$, and another doublet peaks at energy (232.68 eV for Mo $3d_{3/2}$ and 229.1 eV for Mo $3d_{5/2}$) corresponding to semiconducting (2H) phase of $MoSe_2$, while the peaks at 235.74 eV ($3d_{3/2}$) belong to Mo^{6+}. This observation reveals the formation of hybrid 1T (34%) and 2H (66%) contribution of $MoSe_2$ in $MoSe_2$-Ni foam electrode [57, 98-101]. The Se 3d spectrum for $MoSe_2$-Ni foam (**Figure 3.5 (f)**) typically exhibits peaks, corresponding to the Se $3d_{5/2}$ (~54.24 eV) and Se $3d_{3/2}$ (~55.0 eV) along with SeO_x (~58.7 eV and ~59.5 eV) possibly due to the partial oxidation of Se edges [76, 77, 102]. During hydrothermal synthesis of $MoSe_2$ on different substrates such as Ni foam and CCP, the underlying mechanism may vary. One possible reason for the formation of SeOx species during the synthesis on Ni foam but not on CCP could be attributed to the difference in the chemical interactions at the precursors/substrate interface. The Ni foam typically possesses a higher catalytic activity and surface energy compared to conducting carbon paper, which may facilitate the oxidation of selenium at the Ni foam surface. It is also clear that $MoSe_2$-Ni foam has more metallic phase compared to $MoSe_2$-CCP, which may provide better catalytic response of $MoSe_2$-Ni foam.

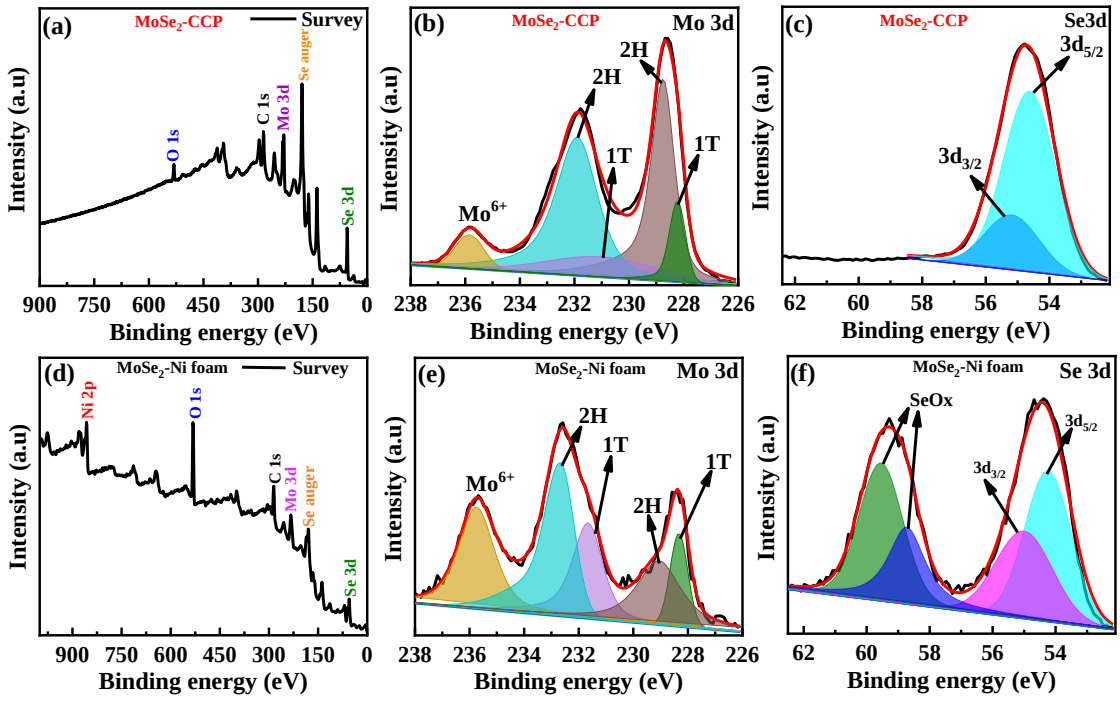

Figure. 3.5 *(a) Survey spectrum, spectra of (b) Mo 3d and (c) Se 3d for $MoSe_2$-CCP; (d) survey spectrum, spectra of (e) Mo 3d and (f) Se 3d, for $MoSe_2$-Ni foam.*

3.4.1.2 Electrochemical Characterization

Electrochemical active surface area

Electrochemical active surface area (ECSA) has been examined to understand the electrocatalytic performance of vertically grown $MoSe_2$-Ni foam (**Figure 3.6 (a,c)**) and $MoSe_2$-CCP (**Figure 3.6 (b,d)**) electrodes in 1M KOH and $MoSe_2$-CCP (**Figure 3.6 (c)**), $MoSe_2$-Ni foam (**Figure 3.6 (d)**) in 0.5M H_2SO_4, respectively

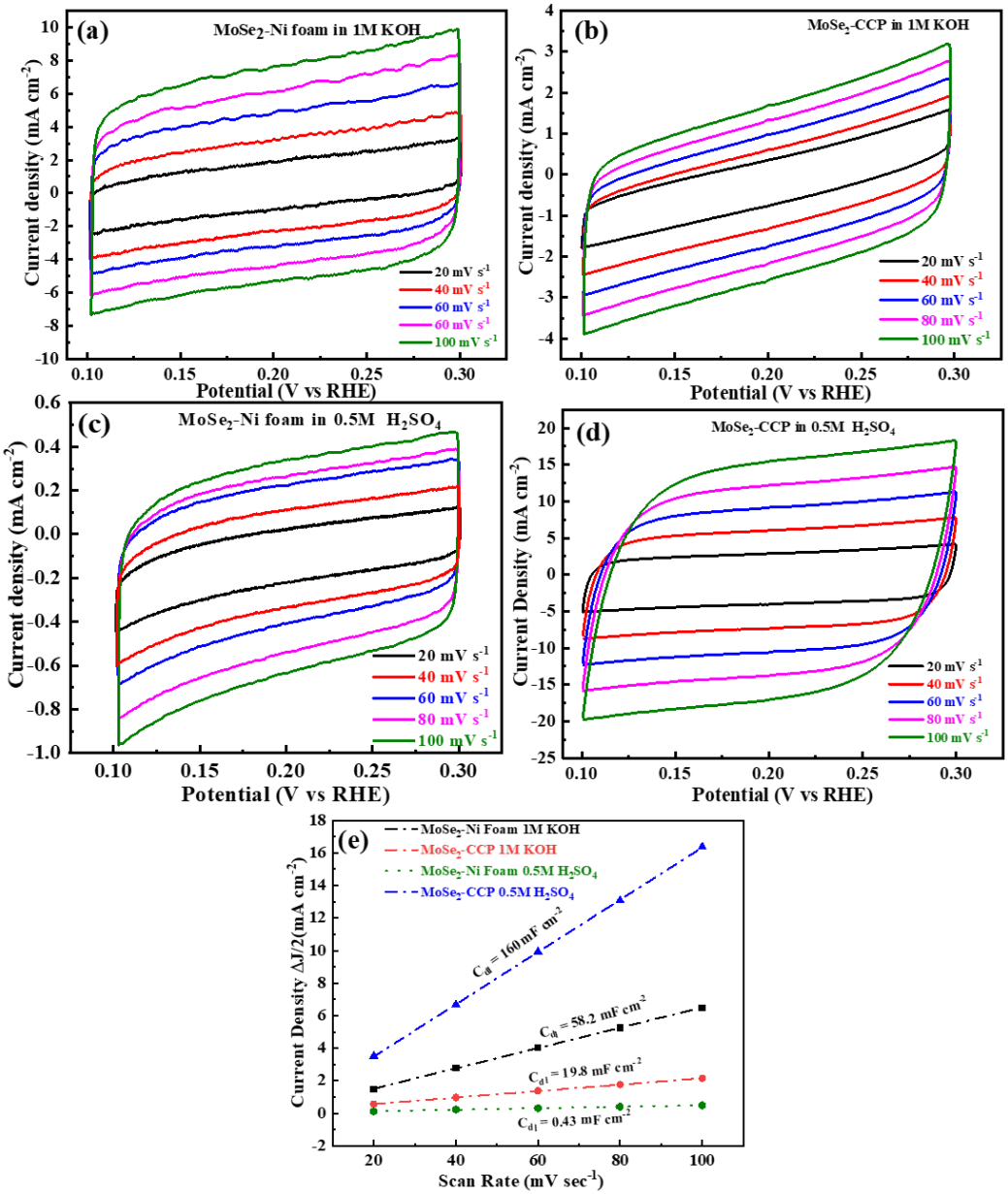

Figure. 3.6 *CV curves of (a) $MoSe_2$-Ni foam and (b) $MoSe_2$-CCP in 1M KOH; (c) $MoSe_2$-Ni foam and (d)$MoSe_2$-CCP in 0.5M H_2SO_4 at different scan rates, (e) current density plotted against different potential sweep rates.*

Cyclic voltammetry (CV) study has been performed at different potential scan rates of (20, 40, 60, 80 and 100 mV s^{-1}) in a capacitive region (non-faradaic) of within a small voltage range (0.1 to 0.3 V vs RHE). The slope of the current density vs. scan rate curve provides double-layer capacitance (C_{dl}). The C_{dl} values of 19.8 and 58.2 mF cm^{-2} are obtained in 1M KOH for $MoSe_2$-CCP and $MoSe_2$-Ni foam, respectively, while $MoSe_2$-CCP and $MoSe_2$-Ni foam show the C_{dl} values of 160 and 0.43 mF cm^{-2} in 0.5M H_2SO_4, as shown in **Figure 3.6 (e)**. The $MoSe_2$-Ni foam shows very low C_{dl} values in 0.5M H_2SO_4 due to the corrosion of Ni foam in acidic environment.

HER activity in basic medium

The LSV curves for HER activity of binder free $MoSe_2$-CCP, $MoSe_2$-Ni foam, 20% Pt/C and bare substrates (Ni foam and CCP) electrodes in 1M KOH at a scan rate of 2 mV s^{-1} are shown in **Figure 3.7 (a)**. Three key reaction steps involved for HER process in the basic electrolyte are given in **equations 3.14-3.16**. The $MoSe_2$-Ni foam exhibits a lower η_{10} ~110 mV and Tafel slope ~82 mV dec^{-1} than $MoSe_2$-CCP (η_{10} ~230 mV and Tafel slope ~98 mV dec^{-1}), bare Ni foam (η_{10} ~355 mV and Tafel slope ~222 mV dec^{-1}) and bare CCP (η_4 ~484 mV and Tafel slope ~355 mV dec^{-1}), as shown in **Figure 3.7 (b)**. Both electrodes ($MoSe_2$-Ni foam and $MoSe_2$-CCP) exhibit good HER performance and comparable to well-established electrocatalysts such as 20% Pt/C (η_{10} ~39 mV and Tafel slope ~42 mV dec^{-1}). The EIS Nyquist plots are obtained to examine the HER kinetics of both electrodes in basic medium at constant potential of -0.2 V vs. RHE, as shown in **Figure 3.7 (c)**. It shows the lower R_S (~1.2 **Ω**) and R_{CT} (~2.6 **Ω**) for $MoSe_2$-Ni foam compared to that for $MoSe_2$-CCP (R_S ~ 2.0 **Ω**, R_{CT} ~ 9.0 **Ω**), suggesting better electrocatalytic activity of $MoSe_2$-Ni foam due to the better electrical conductivity of Ni foam. The iR (90%) compensated LSV curves are shown in **Figure 3.7 (d)** at a potential sweep rate of 2 mV s^{-1} and corresponding iR corrected Tafel plots are given in **Figure 3.7 (e)**. After iR correction, the $MoSe_2$-Ni foam shows even lower η_{10} ~100 mV and

Tafel slope ~73 mV dec^{-1} compared to $MoSe_2$-CCP (η_{10} ~ 220 mV, Tafel slope ~83 mV dec^{-1}). The stability and durability of binder-free electrodes are characterized by the chronoamperometry measurement at a constant overpotential of -0.2V vs. RHE, as shown in **Figure 3.7 (f)**. The $MoSe_2$-Ni foam electrode shows better catalytic stability in alkaline medium (less current reduction ~19%) for 24 h of continuous operation compared to $MoSe_2$-CCP, which shows current reduction of 78% in 20 h.

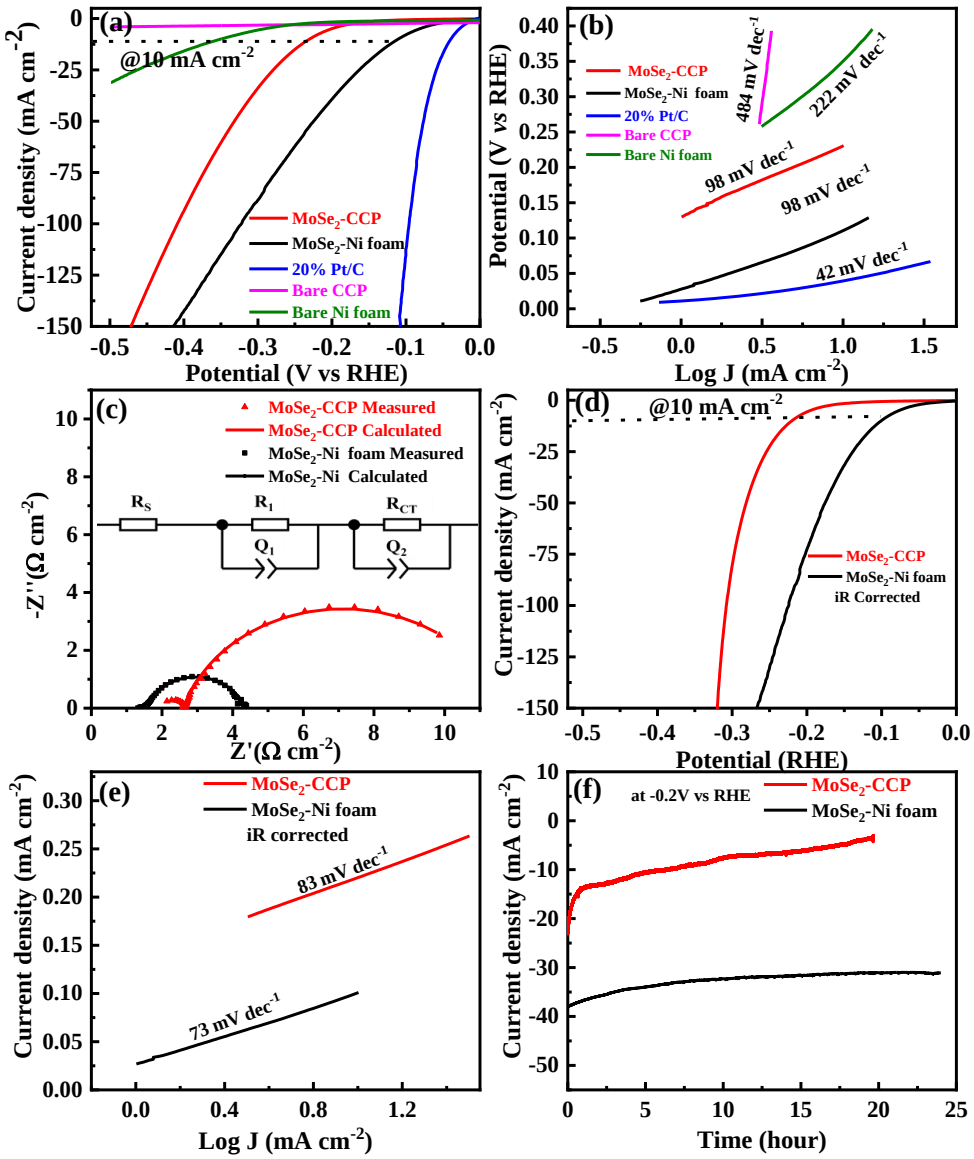

Figure. 3.7 *The HER activity of $MoSe_2$-CCP and $MoSe_2$-Ni foam in 1M KOH (a) LSV curves and (b) corresponding Tafel plots at a potential sweep rate of 2 mV s^{-1}, including for bare substrates and 20%Pt/C(c) EIS curves at a constant overpotential of -0.2 V vs RHE, (d) the iR corrected LSV curves, (e) corresponding iR corrected Tafel plots and (f) chronoamperometry study at a constant overpotential of -0.2 V vs RHE.*

HER activity in acidic medium

We have also performed the LSV measurements in acidic medium (0.5M H_2SO_4) at a scan rate of 2 mV s^{-1} to gain insight into the HER activities of the prepared binder free electrodes, as shown in **Figure 3.8 (a)**. The reactions involved for HER process in acidic medium are provided in **equations 3.11-3.13**. The $MoSe_2$-CCP electrode exhibits the lower overpotential η_{10} ~150 mV than $MoSe_2$-Ni foam (η_{10} ~208 mV), bare CCP (η_{10} ~405 mV) and bare Ni foam (η_{10} ~412 mV). Further, we obtain the corresponding Tafel slopes to elucidate the HER performance of the prepared materials, in acidic medium, as shown in **Figure 3.8 (b)**. The $MoSe_2$-CCP has the lower Tafel slope of 67 mV dec^{-1}, compared to $MoSe_2$-Ni foam (199 mV dec^{-1}). The excellent HER activity of $MoSe_2$-CCP can be attributed to the presence of exposed edges of $MoSe_2$ in vertically grown wrinkled $MoSe_2$ nanosheets. The HER activity of $MoSe_2$-CCP is remarkably comparable to the Tafel slope of the commercially available 20% Pt/C catalyst (η_{10} ~28 mV and Tafel slope ~34 mV dec^{-1}). The EIS has been performed in the frequency range of 1 MHz to 0.01 Hz at constant overpotential (-0.2V) using 5 mV of AC, as shown as in **Figure 3.8 (c)**. The Nyquist plot shows the semicircle-like behavior. Low R_{CT} for $MoSe_2$-CCP (8.5 Ω) than $MoSe_2$-Ni foam (25.5 Ω) and low R_S for $MoSe_2$-CCP (1.4 Ω) than $MoSe_2$-Ni foam (1.8 Ω), suggest better electrocatalytic response of $MoSe_2$-CCP in acidic medium. To assess the actual electrocatalytic effectiveness of the prepared electrodes, an iR correction is applied to compensate potential. **Figure 3.8 (d)** shows the LSV polarisation curves at a scan rate of 2 mV s^{-1} after iR (90%) correction. The corresponding iR corrected Tafel plots are shown in **Figure 3.8 (e)** for all prepared electrodes. We observed that the $MoSe_2$-CCP electrodes displayed the lowest overpotential (η_{10}~ 143 mV) and Tafel's slope (53 mV dec^{-1}), as compared to $MoSe_2$-Ni foam (η_{10}~ 202 mV and Tafel's slope~ 144 mV dec^{-1}). The low performance of $MoSe_2$-Ni foam in acidic medium is due to corrosion of Ni substrate in 0.5M H_2SO_4 [103, 104]. The chronoamperometry has been recorded at constant potential of -0.2V vs

RHE, as shown in **Figure 3.8 (f)**. We observe that $MoSe_2$-CCP shows more stable and durable HER response (~25% current reduction) compared to $MoSe_2$-Ni foam (~66% current reduction) during 24 h of continuous operation. The better performance of binder-free $MoSe_2$-Ni foam and $MoSe_2$-CCP electrodes can be attributed to its wrinkled vertical structure, which provides higher number of exposed edges and hence higher active sites for catalytic activity [105]. Further, CCP and Ni foam substrates provide good electrical conductivity and reduce charge transfer resistance for better catalytic performance of $MoSe_2$ based electrodes.

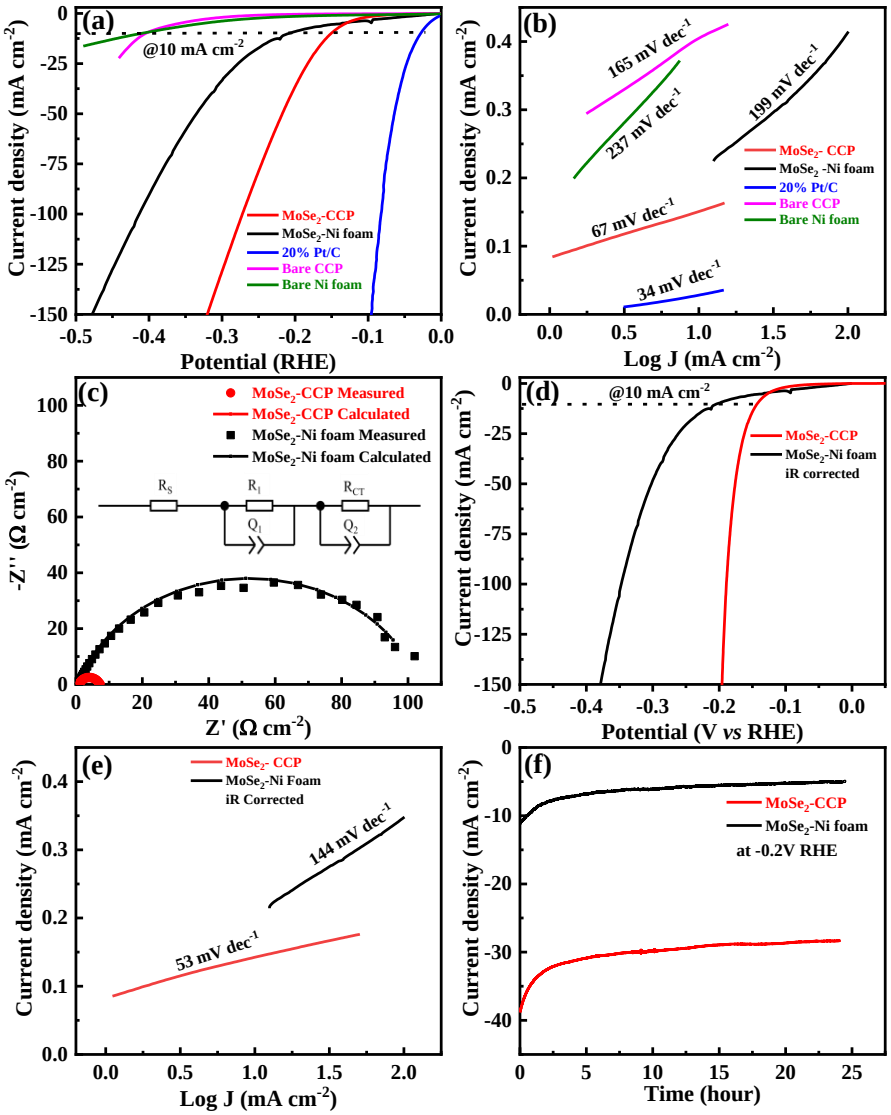

Figure 3.8 *The HER activity of $MoSe_2$-CCP and $MoSe_2$-Ni foam in 0.5M H_2SO_4 (a) LSV curves and (b) corresponding Tafel plots at a potential sweep rate of 2 mV s^{-1}, including for bare substrates and 20%Pt/C(c) EIS curves at a constant overpotential of -0.2 V vs RHE, (d) the iR corrected LSV curves, (e) corresponding iR corrected Tafel plots and (f) chronoamperometry study at a constant overpotential of -0.2 V vs RHE.*

3.4.2 Pristine $MoSe_2$ nanosheets for HER

This study explores the hydrothermally synthesized pristine $MoSe_2$ nanosheets electrocatalyst coated over conducting carbon paper as an electrode for HER. This study delves into the characterization and examination of the electrochemical behavior of pristine $MoSe_2$ nanosheets. To study the HER activity of the prepared samples, we have conducted studies using LSV, EIS and chronoamperometry. Additionally, CV techniques have been employed to determine the ECSA.

3.4.2.1 Characterization of Pristine $MoSe_2$

To understand the morphology and structure of pristine $MoSe_2$ materials, electron microscopy studies are performed. SEM (**Figure 3.9 (a)**) and TEM (**Figure 3.9 (b)**) images for pristine $MoSe_2$ suggest the formation of interconnected wrinkled few layer nanosheets morphology. The high-resolution TEM image (**Figure 3.9 (c)**) clearly shows lattice fringes of layered $MoSe_2$ with thickness of 4 to 5 nm, suggesting the presence of 6-7 layers in each nanosheet stack.

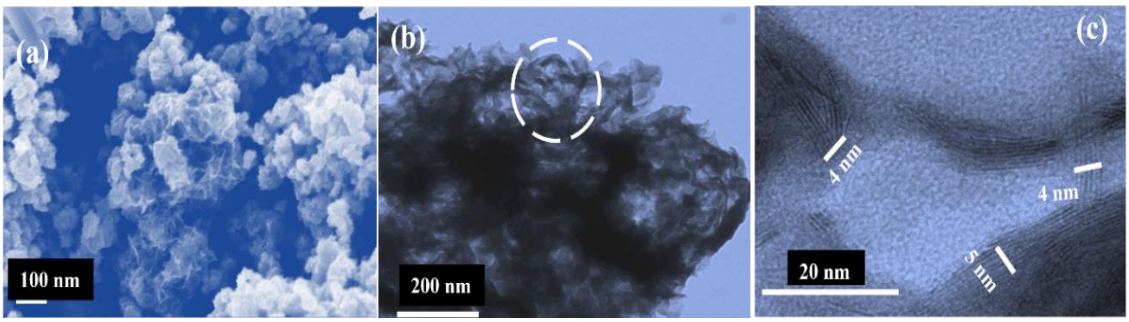

Figure 3.9 *(a) SEM, (b) TEM and (c) HRTEM images of $MoSe_2$ nanosheets.*

The XRD pattern (**Figure 3.10 (a)**) of $MoSe_2$ shows the characteristic peaks at 12.8°, 33.6°, and 55.2°, corresponding to different (h k l) planes of $MoSe_2$ (JCPDS no. 29-0914) [106]. The less intense and broad (002) diffraction peak indicates the formation of few layers in the hexagonally symmetric 2H phase of $MoSe_2$ nanosheets. **Figure 3.10 (b)** shows the

Raman spectrum for pristine $MoSe_2$ nanosheets. The vibrational modes at 237.2 and 285.1 cm^{-1} confirm the presence of A_{1g} and E^1_{2g} modes in $MoSe_2$, associated with out-of-plane and in-plane vibrations of Mo and Se atoms, respectively [79-81]. Along with A_{1g} and E^1_{2g} modes, there is an additional less intense peak, observed around 252 cm^{-1} which manifests defects related to Se^{2-} vacancies in prepared $MoSe_2$ nanosheets, as reported in the literature [107-112]. This may provide good catalytic activity to prepared $MoSe_2$ nanosheets. FTIR spectrum, shown in **Figure 3.10 (c)**, indicates the presence of different functional groups in pristine $MoSe_2$ nanosheets. FTIR spectrum of $MoSe_2$ shows peaks at 818 and 1380 cm^{-1}, corresponding to O-Mo-O and Se-O bonds, respectively. Peaks around 1630 and 3410 cm^{-1}, corresponding to H-O-H bending and O-H stretching under weak hydrogen bonds, respectively [74, 113]. The composition analysis of pristine $MoSe_2$ nanosheets is performed by XPS study. The molybdenum to selenium atomic ratio is found to be approximately 1:1.71, confirming the selenium vacancy defects in prepared $MoSe_2$ nanosheets [114-119]. Figure 3a depicts the survey spectrum of pristine $MoSe_2$, which reveals the existence of characteristic peaks of Mo 3d, Se 3d, and C (carbon peak is due to used carbon tape in measurement).

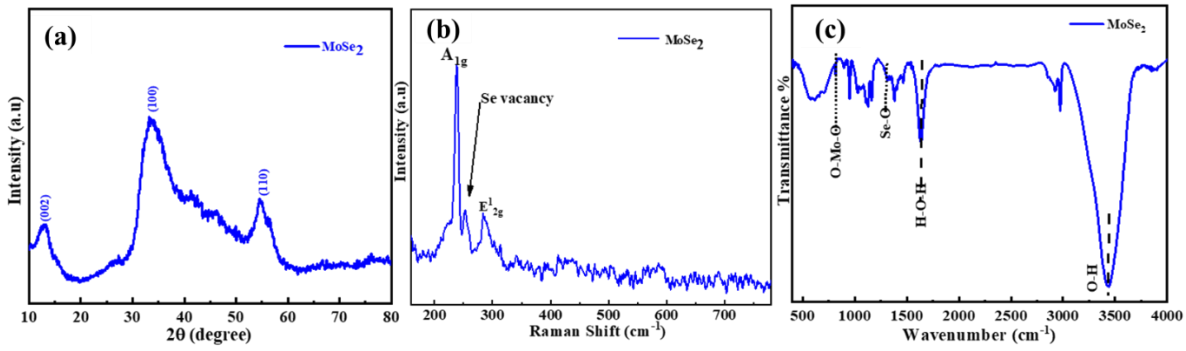

Figure 3.10 *(a) XRD pattern, (b) Raman and (c) FTIR spectra for $MoSe_2$ nanosheets.*

The XPS signal of Mo 3d (Figure 3b) indicates peaks at ~228.4 eV ($3d_{5/2}$) and ~231.5 eV ($3d_{3/2}$) corresponding to Mo^{4+}, while peaks at ~232.6 eV ($3d_{5/2}$) and ~235.7 eV ($3d_{3/2}$) belong to Mo^{6+} [120]. The Se core level XPS spectrum (Figure 3c) shows two distinct peaks at ~54.2 eV for Se $3d_{5/2}$ and ~55.0 eV for Se $3d_{3/2}$, indicating that selenium exists as Se^{2-} state

[114, 121, 122]. These findings reveal that the surface composition of as-synthesized pristine $MoSe_2$ includes Mo^{4+}, Mo^{6+} and Se^{2-}, which is consistent with previous findings for $MoSe_2$.

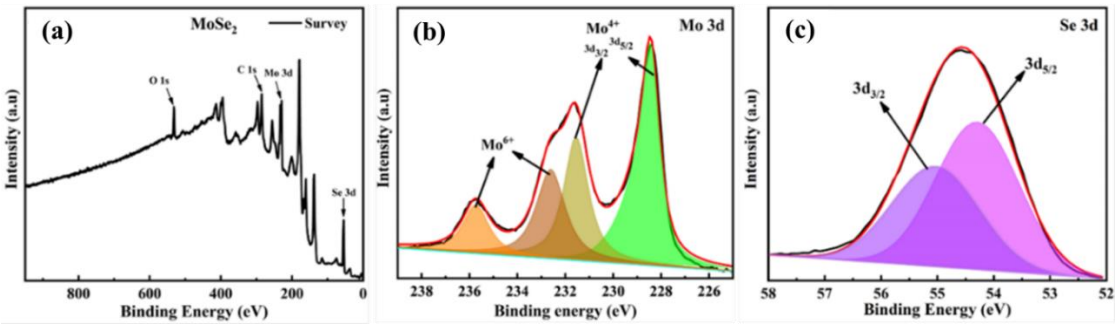

Figure 3.11 *XPS spectra of pristine $MoSe_2$ nanosheets (a) Survey spectrum; Spectra for (b) Mo 3d, and (c) Se 3d.*

3.4.2.2 Electrochemical characterization

In order to understand the electrocatalytic behavior of pristine $MoSe_2$ nanosheets materials, ECSA analysis is performed using the cyclic voltammetry technique [77, 123]. Under a non-faradaic region of 1.2 and 1.25 V (versus RHE), a series of CV scans have been performed at different scan rates (20, 40, 60, 80 and 100 mV s^{-1}) for $MoSe_2$ nanosheets as shown in **Figure 3.12 (a)**. To calculate double-layer capacitance (C_{dl}), the half of the average difference between the average of the anodic and cathodic charging current densities at 1.225 V vs RHE are linearly plotted as a function of scan rates and the slope provides the C_{dl} value [124]. It shows the C_{dl} value of 12.8 mF cm^{-2} equivalent to 3.05 mF cm^{-2} per mg, for $MoSe_2$ nanosheets as shown in **Figure 3.12 (b)**.

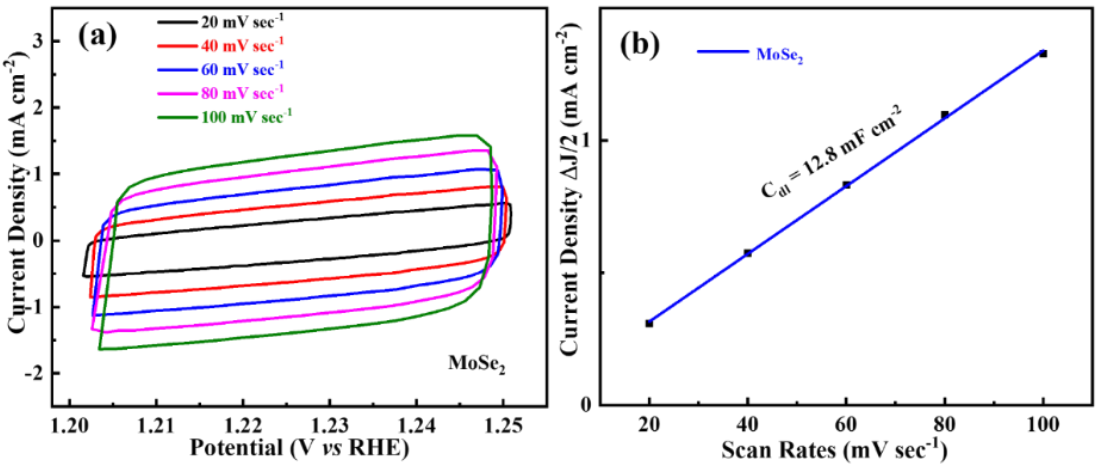

Figure 3.12 *(a) CV curves at different scan rates, (d) current density plotted against different potential sweep rates for pristine $MoSe_2$ nanosheets.*

HER activity in basic medium

The LSV curves for HER catalytic activity of pristine $MoSe_2$ nanosheets 1M KOH at a potential sweep rate of 2 mV s^{-1} is depicted in **Figure 3.13 (a)**. Three key reaction steps involved for HER mechanism in the basic electrolyte are given in **equations 3.14-3.16**. The pristine $MoSe_2$ exhibits low η_{10} ~308 mV and Tafel slope ~211 mV dec^{-1}, as shown in **Figure 3.13 (b)**.

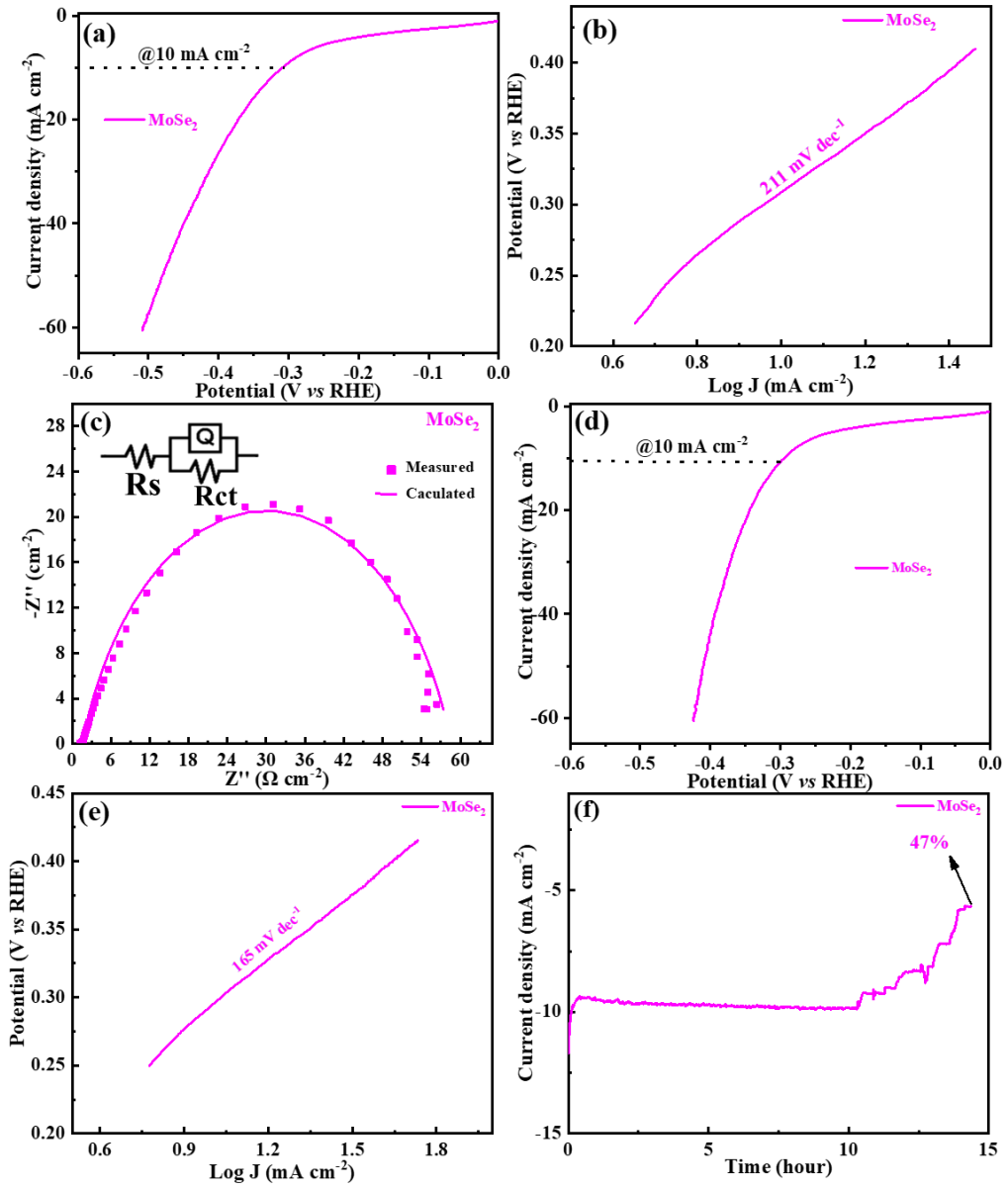

Figure. 3.13 *HER activity of pristine $MoSe_2$ in 1M KOH (a) LSV curve, (b) corresponding Tafel plot (c) EIS spectrum at constant overpotential of -0.2 V vs RHE, (d) The iR corrected LSV curve, (e) corresponding iR corrected Tafel plot, and (f) chronoamperometry study at constant potential of -0.2V vs RHE.*

The EIS has been performed to investigate the HER kinetics of pristine $MoSe_2$ in basic medium at a constant voltage of -0.2 V vs. RHE. The Nyquist plot shows the semicircle like behavior, as shown in **Figure 3.13 (c)**. It shows R_{CT} ~56.5 **Ω**, suggesting significant electrocatalytic activity for pristine $MoSe_2$ due to low charge transfer resistance between electrode and electrolyte. **Figure 3.13 (d)** shows the iR (90%) compensated LSV curve at a potential sweep rate of 2 mV s^{-1} and **Figure 3.13 (e)** provides the corresponding iR corrected Tafel plot. After iR correction, the pristine $MoSe_2$ nanosheets shows lower η_{10} ~294 mV and Tafel slope ~165 mV dec^{-1}. The chronoamperometry experiment at a constant overpotential of -0.2V vs. RHE characterizes the stability and durability of pristine $MoSe_2$, as shown in **Figure 3.13 (f)**. The pristine $MoSe_2$ shows electrocatalytic stability (current retention ~47%) for upto 15 h of continuous operation. The significant HER activity is due to good electrical conductivity of pristine $MoSe_2$ and Se vacancy, which help to reduce the charge transfer resistance.

3.4.3 Ni decorated $MoSe_2$ nanocomposites as electrode for HER

In order to improve the HER activity of $MoSe_2$ nanosheets, we have examined the HER activity of Ni decorated $MoSe_2$ nanocomposites. This study explored the HER activity of Ni nanoparticles decorated over $MoSe_2$ nanosheets (Ni-$MoSe_2$ (5%), Ni-$MoSe_2$ (10%), Ni-$MoSe_2$ (20%)) as electrocatalysts for HER. This study delves into the characterization and examination of the electrochemical behavior of Ni-$MoSe_2$ nanocomposites. To study the HER activity of the prepared samples, we have conducted studies using LSV, EIS and chronoamperometry techniques. Additionally, CV techniques have been employed to determine the ECSA.

3.4.3.1 Characterization of Ni decorated over $MoSe_2$

Electron microscopy is employed to examine the surface morphology of materials synthesized via hydrothermal process. The SEM analysis is conducted on the Ni-$MoSe_2$ (5%),

Ni-$MoSe_2$ (10%) and Ni-$MoSe_2$ (20%) nanocomposites, as shown in **Figure 3.14 (a)**, **Figure 3.14 (b) and Figure 3.14 (c),** respectively. The images indicate the existence of uniformly distributed Ni nanoparticles on $MoSe_2$ nanosheets for all prepared materials. The presence of Mo, Se, Ni elements distribution and chemical composition of Ni-$MoSe_2$ nanocomposites investigated by EDS spectra, as shown in **Figure 3.14 (d-f)**, indicating the purity of nanocomposites. It confirms the presence of nearly same wight percentage of Ni as planned in the synthesis procedure of the nanocomposites.

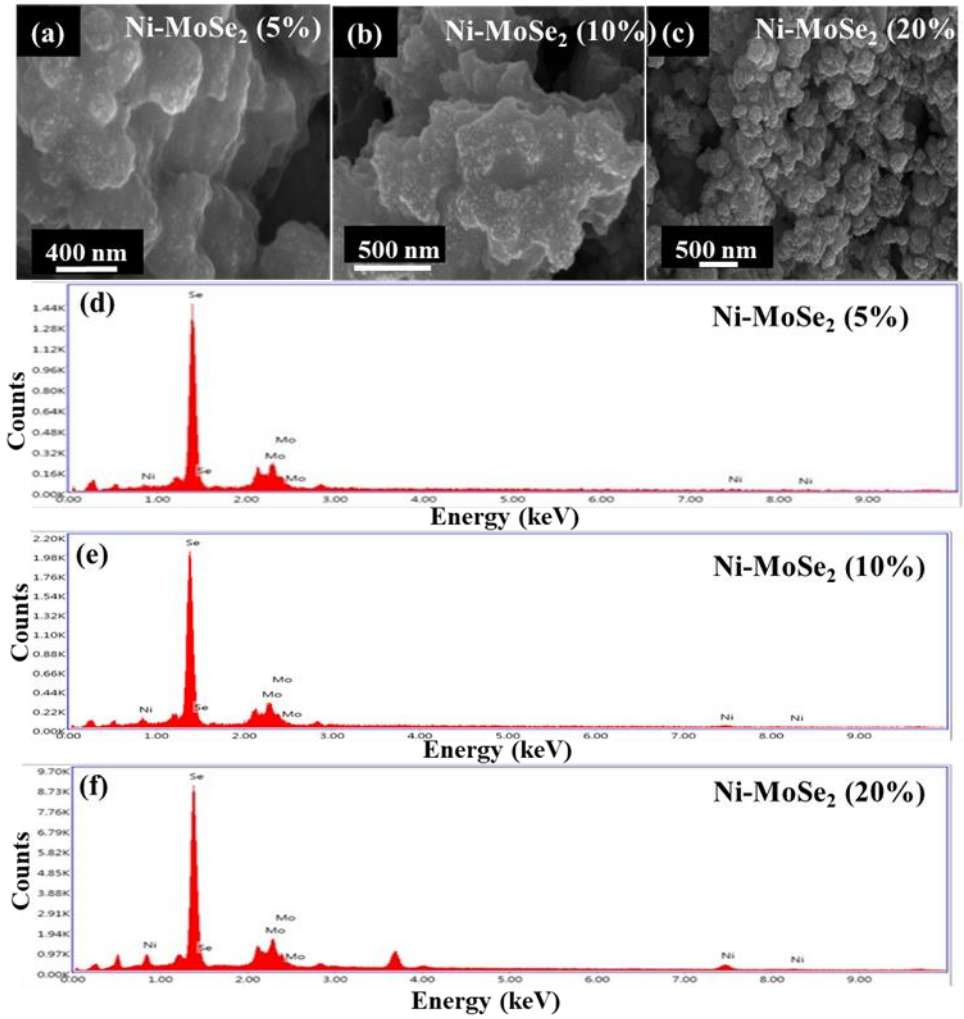

Figure 3.14 *(a,b,c) SEM images and (d,e,f) EDS spectra for Ni-$MoSe_2$ (5%), Ni-$MoSe_2$ (10%), and Ni-$MoSe_2$ (20%) nanocomposites, respectively.*

Further, the TEM image (**Figure 3.15 (a)**) and higher magnification TEM image (**Figure 3.15 (b)**), clearly illustrating the Ni nanoparticles on the $MoSe_2$ nanosheets in Ni-

$MoSe_2$ (10%) nanocomposite. All prepared nanocomposites show uniform phase and distribution of Ni nanoparticle over $MoSe_2$ nanosheets. Then we have done the TEM and XPS studies of one of the nanocomposites i.e Ni-$MoSe_2$ (10%). The TEM images (**Figure 3.15 (a,b)**) of Ni-$MoSe_2$ (10%) clearly confirm the uniform distribution of Ni nanoparticles over $MoSe_2$ nanosheets.

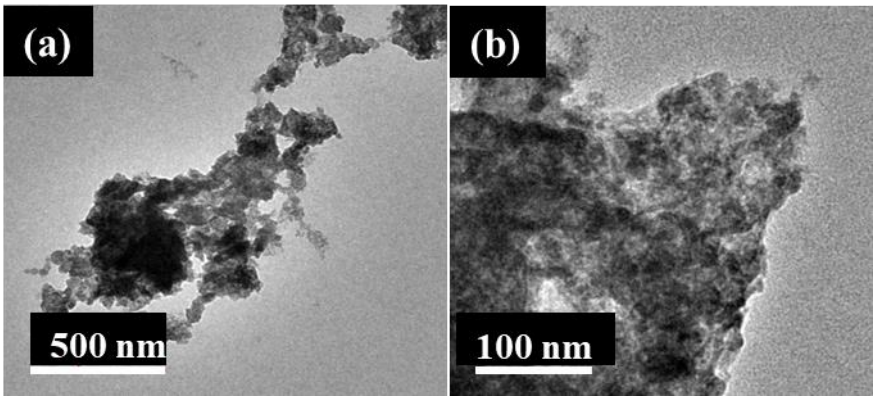

Figure 3.15 *(a) TEM and (b) higher magnification TEM images of Ni-$MoSe_2$ (10%) nanocomposite.*

The XRD patterns of synthesized Ni-$MoSe_2$ nanocomposites (Ni-$MoSe_2$ (5%), Ni-$MoSe_2$ (10%) and Ni-$MoSe_2$ (20%)) exhibit diffraction patterns corresponding to various crystallographic planes of the Ni and $MoSe_2$, as shown in **Figure 3.16 (a)**. The peak appearing at ~31.7° in Ni-$MoSe_2$ (5%) and ~33.4° in Ni-$MoSe_2$ (10%), ~33.5° in Ni-$MoSe_2$ (20%) nanocomposites, attributes to the (100) diffraction plane of $MoSe_2$ [92]. Another peak appearing at ~56.0° for Ni-$MoSe_2$ (5%) and ~55.9° for Ni-$MoSe_2$ (10%), ~55.8° for Ni-$MoSe_2$ (20%), attributes to the (110) diffraction plane of $MoSe_2$, while a peak around ~44° in Ni-$MoSe_2$ (5%), Ni-$MoSe_2$ (10%) and Ni-$MoSe_2$ (20%), attributed to the (111) plane of Ni nanoparticle. Raman spectroscopy serves as tool to investigate the vibrational information of synthesized Ni-$MoSe_2$ nanocomposites based materials. Raman spectra depicted in **Figure 3.16 (b)**, confirm the existence of vibrational modes of $MoSe_2$ in prepared Ni-$MoSe_2$ nanocomposites. The peaks at ~236.8 for Ni-$MoSe_2$ (5%), ~235.6 for Ni-$MoSe_2$ (10%) and ~236.8 for Ni-$MoSe_2$ (20%) depict the in-plane (A_{1g}) while, peak at ~282.1 for Ni-$MoSe_2$ (5%),

~280.8 for Ni-$MoSe_2$ (10%) and ~279.7 for Ni-$MoSe_2$ (20%) is attributed to out-of-plane (E^1_{2g}) vibrations of Mo and Se atoms [73, 79, 95]. FTIR spectra (**Figure 3.16 (c)**) show multiple peaks corresponding to different molecular vibrations in Ni-$MoSe_2$ (5%), Ni-$MoSe_2$ (10%) and Ni-$MoSe_2$ (20%) nanocomposites. The peaks around 857, 1031, 1629, and 3466 cm^{-1} are belonging to the O-Mo-O, M=O, Mo-Se and O-H vibrations, respectively [68, 76, 96, 97].

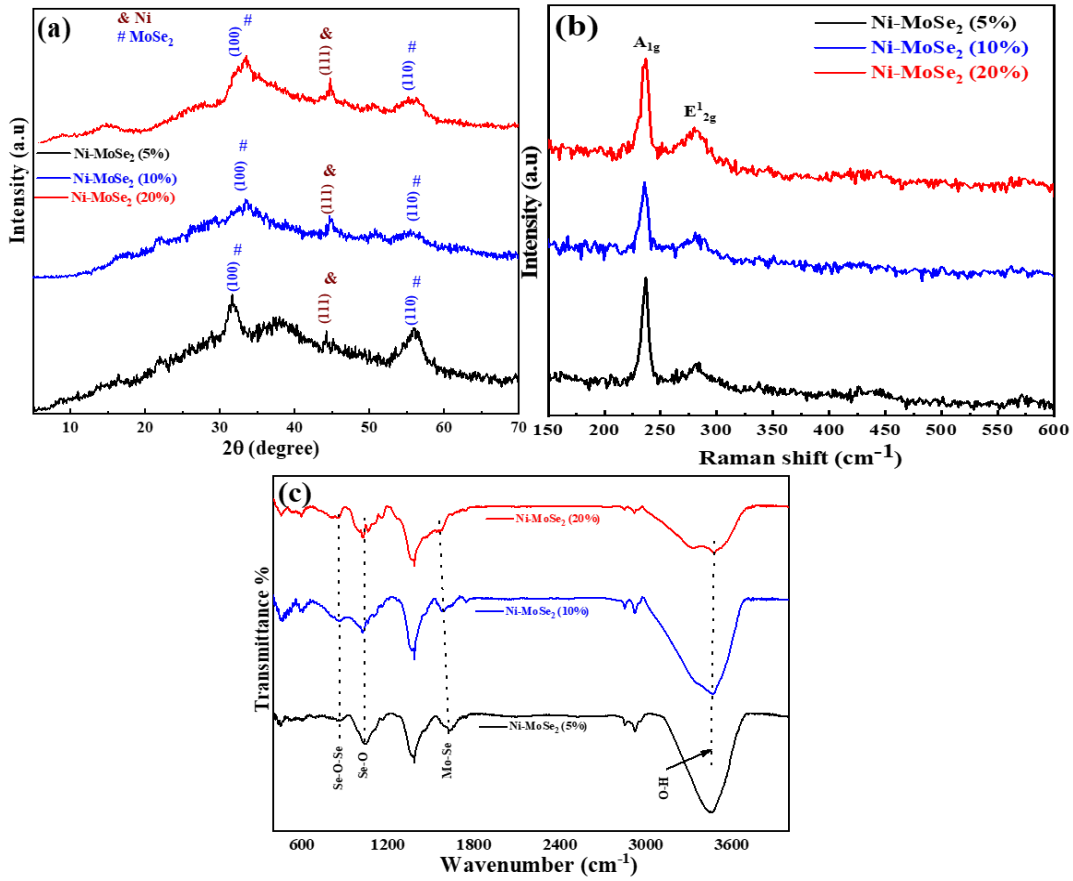

Figure 3.16 *(a) XRD patterns, (b) Raman and (c) FTIR spectra for Ni-$MoSe_2$ (5%), Ni-$MoSe_2$ (10%) and Ni-$MoSe_2$ (20%) nanocomposites.*

XPS survey spectrum, conducted on the Ni-$MoSe_2$ (10%) sample, reveals the typical peaks of Mo-3d, Se-3d, Ni-2p, C, and O, as depicted in **Figure 3.17 (a)**. The Mo-3d spectrum (**Figure 3.17 (b)**) of the Ni-$MoSe_2$ (10%) has a couple of doublet peaks at 231.8 eV for Mo $3d_{3/2}$ and 228.7 eV for Mo $3d_{5/2}$ corresponding to Mo^{4+} coordination of $MoSe_2$, and another doublet peaks at energy (232.3 eV for Mo $3d_{5/2}$ and 232.3 eV for Mo $3d_{3/2}$) belongs to Mo^{6+} of MoOx formation. Selenium exists in the Se^{2-} form, as seen by the two different peaks in the Se core

level XPS spectrum (**Figure 3.17 (c)**), which are located at approximately 54.1 eV ($3d_{5/2}$) and 54.9 eV ($3d_{3/2}$), along with SeO_x (~58.4 eV and ~59.5 eV) possibly due to the partial oxidation of Se edges [76, 77, 102]. Peaks of the Ni 2p spectrum are fitted to two spin-orbit doublets and two shakeup satellite peaks, as shown in **Figure 3.17 (d)**. Binding energies of ~853.8 (Ni^{3+}) and ~855.8 eV (Ni^{2+}) are ascribed to Ni $2p_{3/2}$, whereas peaks with binding energies of ~871.2 (Ni^{3+}) and ~873.6 eV (Ni^{2+}) are assigned to Ni $2p_{1/2}$ peaks.

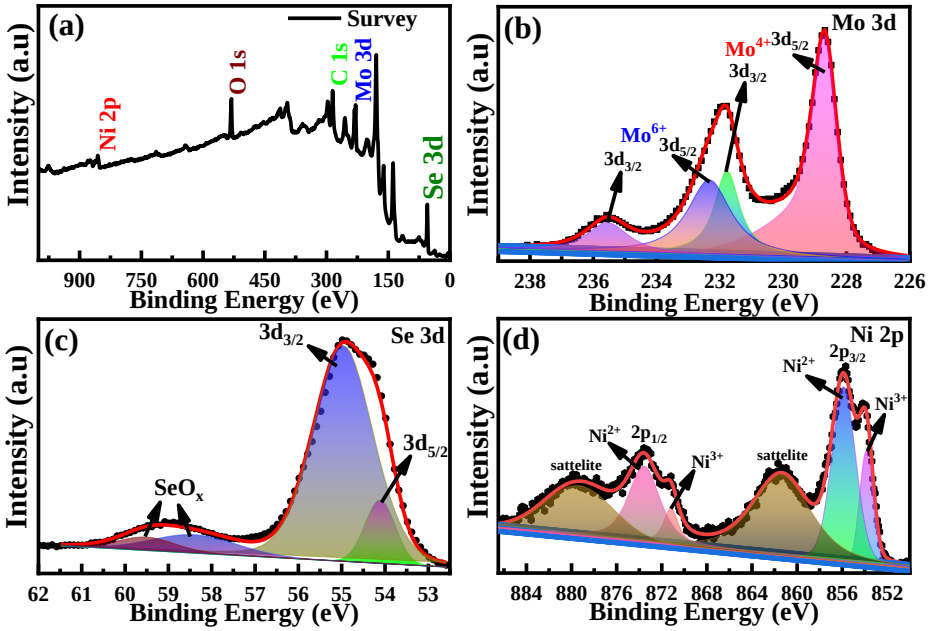

Figure 3.17 *(a) Survey spectrum; spectra of (b) Mo 3d, (c) Se 3d and (d) Ni 2p, for Ni-$MoSe_2$ (10%) nanocomposite.*

3.4.3.2 Electrochemical characterization

ECSA has been examined to understand the electrocatalytic performance of Ni-$MoSe_2$ (5%) (**Figure 3.18 (a)**), Ni-$MoSe_2$ (10%) (**Figure 3.18 (b)**) and Ni-$MoSe_2$ (20%) (**Figure 3.18 (c)**), in 1M KOH. CV study has been performed at different potential scan rates of (20, 40, 60, 80 and 100 mV s^{-1}) in a capacitive region (non-faradaic) within a small voltage range (0.1 to 0.3 V vs RHE). The slope of the current density vs. scan rate curve provides double-layer capacitance (C_{dl}), as shown in **Figure 3.18 (d)**. The C_{dl} values of 29, 32.2, and 23 mF cm^{-2} are obtained Ni-$MoSe_2$ (20%), Ni-$MoSe_2$ (10%) and Ni-$MoSe_2$ (5%), respectively in 1M KOH, as

shown in **Figure 3.18 (e)**. The higher C_{dl} for Ni-$MoSe_2$ (10%) suggests the higher ECSA compared to other Ni-$MoSe_2$ nanocomposites.

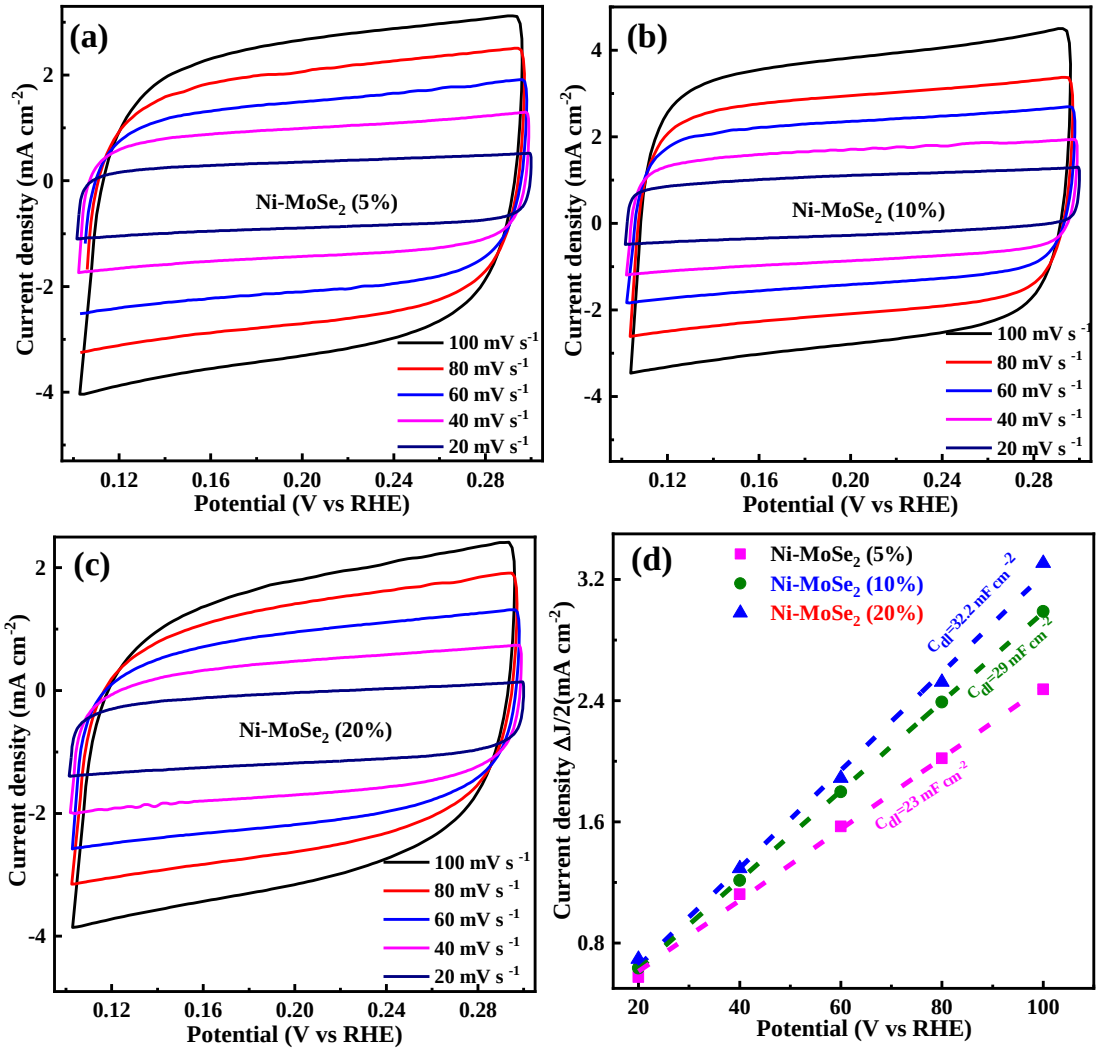

Figure 3.18 *CV curves of (a) Ni-$MoSe_2$ (5%) and (b) Ni-$MoSe_2$ (10%) and (c) Ni-$MoSe_2$ (20%) in 1M KOH at different scan rates and (e) current density plotted against different potential sweep rates.*

HER activity in basic medium

The LSV curves for HER catalytic activity of Ni-$MoSe_2$ nanocomposites in 1M KOH at a potential sweep rate of 2 mV s^{-1} are depicted in **Figure 3.19 (a)**. The Ni-$MoSe_2$ (10%) exhibits a lower η_{10} ~141 mV and Tafel slope ~70 mV dec^{-1} than Ni-$MoSe_2$ (5%) [η_{10} ~188 mV and Tafel slope ~107 mV dec^{-1}] and Ni-$MoSe_2$ (20%) [η_{10} ~177 mV and Tafel slope ~90 mV dec^{-1}], as shown in **Figure 3.19 (b)**. The Ni-$MoSe_2$ (10%) shows the exhibit better HER

performance among Ni-$MoSe_2$ nanocomposites based materials. The EIS Nyquist plots are generated to investigate the HER kinetics of both electrodes in basic medium at a constant voltage of -0.2 V vs. RHE, as shown in **Figure 3.19 (c)**. It shows the lower R_{CT} (~4.0 **Ω**) for Ni-$MoSe_2$ (10%) compared to Ni-$MoSe_2$ (5%) (R_{CT} ~23.0 **Ω**) and Ni-$MoSe_2$ (20%) (R_{CT} ~ 13.0 **Ω**), suggesting better electrocatalytic activity of Ni-$MoSe_2$ (10%) due to the optimal decoration of Ni nanoparticle over $MoSe_2$, which provide higher synergistic effect between them. **Figure 3.19 (d)** shows the iR (90%) compensated LSV curves at a potential sweep rate of 2 mV s^{-1} and **Figure 3.19 (e)** provides the corresponding iR corrected Tafel plots. After iR correction, the Ni-$MoSe_2$ (10%) shows even lower η_{10} ~141 mV and Tafel slope ~60 mV dec^{-1} compared to Ni-$MoSe_2$ (20%) (η_{10} ~ 163 mV, Tafel slope ~76 mV dec^{-1}) and Ni-$MoSe_2$ (5%) (η_{10} ~ 170 mV, Tafel slope ~84 mV dec^{-1}). The chronoamperometry experiment at a constant overpotential of -0.2V vs. RHE characterizes the stability and durability of Ni-$MoSe_2$ nanocomposites-based electrodes, as shown in **Figure 3.19 (f)**. The Ni-$MoSe_2$ (10%) electrode shows better catalytic stability (current retention ~96%) for 24 h of continuous operation compared to Ni-$MoSe_2$ (20%) (~63%) for 24 h and Ni-$MoSe_2$ (5%) (~56%) for 15 h. The higher HER activity for Ni-$MoSe_2$ (10%) is due to the optimum presence of Ni atoms over $MoSe_2$. It provides a high synergistic effect compared to Ni-$MoSe_2$ (20%) and Ni-$MoSe_2$ (5%).

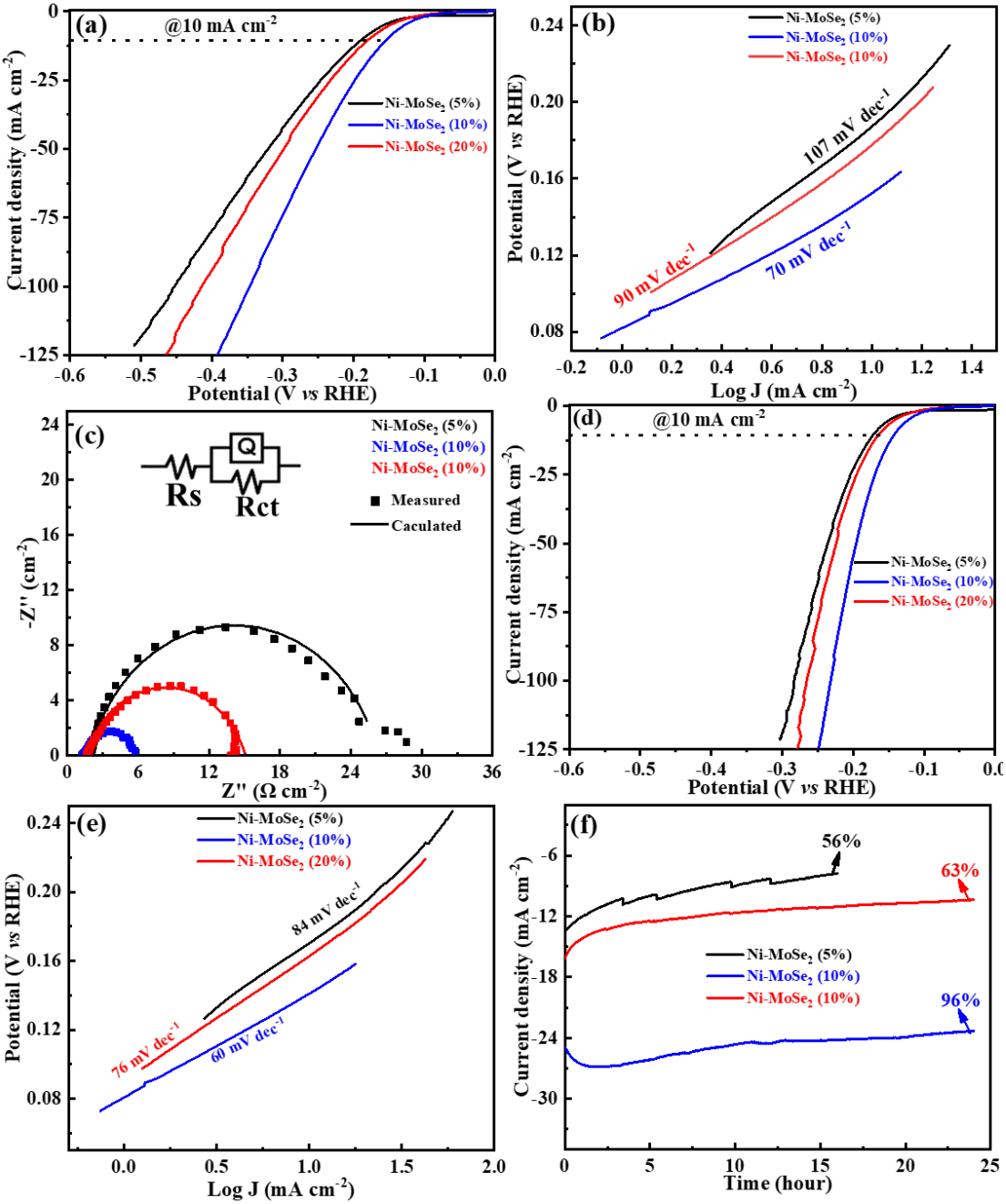

Figure. 3.19 *(a) LSV curves, (b) corresponding Tafel plots at scan rates of 2 mV s^{-1}, (c) EIS spectra at constant overpotential of -0.2 V vs RHE, (d) The iR corrected LSV curves, (e) corresponding iR corrected Tafel plots and (f) chronoamperometry study at constant potential of -0.2V vs RHE of Ni-$MoSe_2$ (5%), Ni-$MoSe_2$ (10%) and Ni-$MoSe_2$ (20%) nanocomposites in 1M KOH.*

The HER activity of prepared binder-free electrodes ($MoSe_2$-CCP and $MoSe_2$-Ni foam), pristine $MoSe_2$, and Ni decorated over $MoSe_2$ (Ni-$MoSe_2$ (20%), Ni-$MoSe_2$ (10%), Ni-$MoSe_2$ (5%)) have been summarized in **Table 3.1**.

Table 3.1 The comparative performance summary of HER activity of our studied materials.

Electrocatalyst/ electrode	**Overpotential (η_{10})**	**Electrolyte**	**Tafel slope (mV dec^{-1})**	**Ref.**
$MoSe_2$-CCP	83	1M KOH	220	This work
$MoSe_2$-Ni foam	**73**	**1M KOH**	**100**	This work
$MoSe_2$-CCP	**53**	**0.5M H_2SO_4**	**143**	This work
$MoSe_2$-Ni foam	144	0.5M H_2SO_4	202	This work
Pristine $MoSe_2$	165	1M KOH	294	This work
5% Ni- $MoSe_2$	84	1M KOH	170	This work
10% Ni-$MoSe_2$	**60**	**1M KOH**	**141**	This work
20% Ni-$MoSe_2$	76	1M KOH	163	This work
$MoSe_2$/$Co_{0.85}Se$/NF	102	0.5M H_2SO_4	35	[125]
MoO_2/$MoSe_2$-CC	181	0.5M H_2SO_4	49.1	[126]
Insitu $MoSe_2$@Mo	121	1M KOH	71	[127]
Pt/C	20.7	1M KOH	43	[128]

3.5 Conclusion

This chapter presents the HER activity of binder free $MoSe_2$ grown over different conducting substrates ($MoSe_2$-CCP, $MoSe_2$-Ni foam) electrodes, pristine $MoSe_2$ nanosheets and Ni decorated $MoSe_2$ nanocomposites (Ni-$MoSe_2$ (20%), Ni-$MoSe_2$ (10%), Ni-$MoSe_2$ (5%)) based electrodes for HER activity. The ECSA, overpotential, Tafel slope, charge transfer resistance and electrocatalytic stability are measured and compared. The results reveal that the $MoSe_2$-Ni foam shows best HER activity (η_{10} ~100 mV and Tafel slope ~73 mV dec^{-1}) in basic medium among studied materials. While $MoSe_2$-CCP shows highest electrocatalytic activity for HER in acidic medium (η_{10}~ 143 mV, Tafel's slope ~53 mV dec^{-1}), among studied materials. The low performance of $MoSe_2$-Ni foam in acidic medium is due to the continuous

dissolution of Ni foam in 0.5M H_2SO_4 during continuous HER operation, resulting in corrosion of the Ni substrate in an acidic medium. The better performance of binder-free $MoSe_2$-Ni foam and $MoSe_2$-CCP electrodes can be attributed to their wrinkled vertical structure, which provides higher number of exposed edges and reduces charge transfer resistance, hence higher active sites for catalytic activity. Further, Ni-$MoSe_2$ nanocomposites (Ni-$MoSe_2$ (20%), Ni-$MoSe_2$ (10%), Ni-$MoSe_2$ (5%)) based materials have been HER activity in 1M KOH. Ni-$MoSe_2$ (10%) shows lower η_{10} ~141 mV and Tafel slope ~60 mV dec^{-1} compared to Ni-$MoSe_2$ (20%), Ni-$MoSe_2$ (5%) and pristine $MoSe_2$. The higher HER activity for Ni-$MoSe_2$ (10%) is due to the optimum presence of Ni atoms over $MoSe_2$, which provides a high synergistic effect between $MoSe_2$ and Ni. The Pristine $MoSe_2$ shows significant HER activity, which has been improved by making nanocomposite with Ni decoration over $MoSe_2$ nanocomposites.